Research Square

Preprints are preliminary reports that have not undergone peer review.
They should not be considered conclusive, used to inform clinical practice,
or referenced by the media as validated information.

C3N4/C3N5 homojunction induced peroxymonsulfate activation for efficient oxidation of sulfamethoxazole

Chi Zhou
Hubei Water Resources Research Institute
Xuwei Deng
Institute of Hydrobiology
Hanmei zhao
HuBei Water Conservancy Technical College
Hongyan song
South central Minzu University
Dongqin Wang
Wuhan Second Ship Design and Research Institute
Laiyan Wu
wulaiyan@scuec.edu.cn

South central Minzu University

Research Article

Keywords: Graphitic carbon nitride, Heterojunction, PMS Activation, SMX degradation, visible illustration

Posted Date: March 25th, 2026

DOI: https://doi.org/10.21203/rs.3.rs-9153847/v1

License: This work is licensed under a Creative Commons Attribution 4.0 International License.
Read Full License

Additional Declarations: No competing interests reported.

C_3N_4/C_3N_5 homojunction induced peroxymonsulfate activation for efficient oxidation of sulfamethoxazole

Chi Zhou[a1], Xuwei Deng[b1], Hanmei Zhao[c], Hongyan Song[d], Dongqin Wang[e], Laiyan Wu[d*]

a Hubei Water Resources Research Institute, Hubei Water Resources and Hydropower Science and Technology Promotion Center Wuhan, 430070, China

b Institute of Hydrobiology, Chinese Academy of Sciences, Wuhan, 430072, China

c HuBei Water **Conservancy** Technical College, Wuhan, 430072, China

d College of Resources and Environmental Science, South-Central Minzu University, Wuhan 430074, China

e Wuhan Second Ship Design and Research Institute, Wuhan China 430205

*Corresponding author: wulaiyan@scuec.edu.cn

Abstract

As a widely used sulfonamide antibiotic, Sulfamethoxazole (SMX) poses considerable environmental risks for its persistence and antibio-degradability in aquatic ecosystems. Although Peroxymonosulfate (PMS)-based advanced oxidation processes show promise in antibiotic removal, metal-based activators often suffer from leaching and stability issues. Here, a novel metal-free C_3N_4/C_3N_5 homojunction (rCN-AT) photocatalyst was synthesized via KBr-assisted thermal polymerization using cyanuric acid and 3-amino-1,2,4-triazole as precursors, for visible-light-driven PMS activation. The rCN-AT/PMS/Vis system achieved 99.98% SMX degradation within 45 min with the visible light irradiation, significantly outperforming C_3N_4/PMS/Vis (28.85%), C_3N_5/PMS/Vis s (33.92%), and CN-AT/PMS/Vis (83.64%). The enhanced activity is attributed to the homojunction structure and large specific surface area of rCN-AT, which facilitate efficient charge separation and promote PMS adsorption/activation. Electronic band structure determination indicates PMS acts as an efficient electron acceptor, improving photogenerated electron transfer efficiency. EPR analysis revealed the involvement of $SO_4^{\cdot-}$, ·OH, $\cdot O_2^-$,$^1O_2$ and h^+. Among these**,** h^+, $\cdot O_2^-$ and $^1O_2$ were identified as the dominant species, indicating that both radical and non-radical pathways contribute to SMX degradation. This work provides an efficient metal-free homojunction photocatalyst and offers new insights into PMS activation mechanisms, which are valuable for the treatment of antibiotic-contaminated water.

Keywords: Graphitic carbon nitride; Heterojunction; PMS Activation; SMX degradation; visible illustration.

1. Introduction

Sulfamethoxazole (SMX) is extensively applied as sulfonamide antibiotic for treating infections in humans and animals [1, 2]. However, due to overuse and improper wastewater disposal, SMX persists in aquatic environments [3-6], even at trace concentrations, and exerts adverse effects on public health and environmental ecosystems [7]. Owing to its anionic property and antimicrobial activity, conventional biological wastewater treatments (e.g., biodegradation and biosorption) are inefficient for SMX removal [8]. Thus, efficient and environmentally benign methods for SMX elimination from water sources are urgently required.

Recently, advanced oxidation processes (AOPs) based on peroxymonsulfate (PMS) have been proposed as effective technologies for eliminating organic contaminants, as they generate reactive radicals (e.g. sulfate radicals ($SO_4^{\cdot-}$) and hydroxyl radicals ($\cdot OH$) or non-radical species (e.g. single oxygen ($^1O_2$) and surface-bound complexes) [9, 10].

Various activation strategies, including thermal [11], alkaline[12], UV[13], ultrasound[14], semiconductors[15-18], carbon catalysts[19] and electrochemical methods[20], have been employed to activate PMS. While metal-based cocatalysts (e.g., Co, Mn, Fe ions/oxides) are preferred for their cost-effectiveness compared to energy-based activation [13], they suffer from metal leaching and poor stability, hindering practical applications. Consequently, the development of environmentally friendly metal-free catalysts for PMS activation has emerged as a research hotspot.

Graphitic carbon nitrides (e.g., C3N4) are promising metal-free semiconductors, but their poor photocatalytic performance (due to rapid charge recombination) requires coupling with other materials (e.g., PTCDA [21], $FeCo_2S_4$ [22], TiO_2 [23], MOF[24], Co[25]). In contrast, g-C3N5 exhibits superior properties, including a narrower band gap (2.00 eV vs. 2.80 eV for C3N4), a more negative conduction band potential (-1.46 V vs. -1.23 V for C3N4), higher visible-light utilization efficiency, and longer photogenerated carrier lifetime[26-29]. The band structure difference between g-C3N4 and g-C3N5 favors the formation of interlaced energy bands, promoting spatial charge separation. However, constructing heterojunctions on C3N4 often disrupts its structure and hinders carrier transfer[30]. Thus, fabricating a C3N4/C3N5 homojunction may address these limitations.

This study synthesized a porous C3N4/C3N5 homojunction named rCN-AT via KBr-assisted thermal polymerization. The specific objectives are: (1) to characterize the morphology, structure, and photoelectrochemical properties of rCN-AT; (2) to investigate factors influencing SMX removal (e.g., pH, temperature, catalyst dosage) and catalyst stability. (3) to evaluate its performance in activating PMS for SMX degradation under visible light; (4) to identify dominant reactive species and clarify the degradation mechanism;

The novelty lies in the KBr-induced hierarchical porous structure and homojunction synergy, which enhance PMS activation efficiency and avoid metal-related issues.

2. Experimental section

2.1Materials Cyanuric acid ($C_3H_3N_3O_3$, ⩾96.0%), 3-amino-1,2,4-triazole ($C_2H_4N_4$, ⩾96.0%), potassium bromide (KBr, ⩾99.0%), peroxymonosulfate (PMS, ⩾99.0%), sulfamethoxazole (SMX, ⩾98.0%), and other reagents were purchased from Aladdin Reagent Co., Ltd. (Shanghai, China) and used without further purification. Deionized water was used throughout the experiments.

2.2 Sample preparation.

2.2.1 ***Synthesis of Pristine*** *C3N4, C3N5 and CN-AT.* For pristine C3N4, 3.0 g of cyanuric acid was placed in an alumina crucible, heated to 500 °C at a ramping rate of 10 °C·min^{-1}, and calcined for 3 h. The product was ground into a powder. For pristine C3N5, 3.0 g of 3-amino-1,2,4-triazole was calcined under the same conditions as C3N4. While for CN-AT homojunction, A mixture of 3.0 g cyanuric acid and 3.0 g 3-amino-1,2,4-triazole was calcined at 500 °C for 3 h (ramping rate: 10 °C·min^{-1}).

2.2.2 Synthesis of rCN-AT. 3.0 g of cyanuric acid and 3.0 g of 3-amino-1,2,4-triazole were separately dissolved in KBr solution (0.20 g·mL^{-1}). The solutions were evaporated to dryness at 80 °C, and the resulting solids were ground, mixed, and calcined at 500 °C for 3 h (ramping rate: 10 °C·min^{-1}). The final product was labeled rCN-AT after drying for 12 h .

2.3. Characterization Detailed characterization methods are provided in the Supplementary Information.

2.4 Photocatalytic activity evaluation. SMX degradation experiments were conducted in a 50 mL quartz reactor. Typically, 25 mg of catalyst was dispersed in 25 mL of SMX solution (10 μM). The suspension was stirred in the dark for 30 min to reach adsorption-desorption equilibrium. Then, 0.15 mL of PMS solution (0.05 mol·L^{-1}) was added, and the reaction was triggered by turning on the 350 W xenon lamp. At predetermined intervals, 1 mL of suspension was sampled and mixed with 0.15 mL of 0.05 mol·L^{-1} $Na_2S_2O_3$ to quench the reaction. The supernatant was collected via centrifugation (8000 rpm, 5 min) and analyzed using a high-performance liquid chromatograph (HPLC, Thermo Fisher Scientific U3000) with a C18 column (250 × 4.6 mm, 5 μm). The mobile phase was methanol:water (60:40, v/v) at a flow rate of 1.0 mL·min^{-1}, and the detection wavelength was 268 nm.

2.5 Radical quenching experiments, Stability and Reusability Tests. Methanol (MeOH), tert-butanol (TBA), p-benzoquinone (p-BQ), furfuryl alcohol (FFA) and ethylenediaminetetraacetic acid disodium salt (EDTA-2Na)

were used as scavengers of the $SO_4^{\cdot-}$, $\cdot OH$, $\cdot O_2^-$, $^1O_2$ and h^+, respectively [22, 31, 32]. The stability of rCN-AT was evaluated via five consecutive degradation cycles. After each cycle, the used catalyst was firstly centrifugated and washed three times by deionized water and ethanol, the collections were dried at 60 °C for 12 h.

2.6 Influence Factor Experiments. The effects of initial pH (3.16–11.06), rCN-AT dosage (0.1–2.0 $g \cdot L^{-1}$), PMS dosage (0.05–0.3 mM), initial SMX concentration (5–20 μM), temperature (25–45 °C), and coexisting anions (Cl^-, HCO_3^-, $H_2PO_4^{2-}$, NO_3^-, and SO_4^{2-}, 10 mM) on SMX degradation were investigated. The pseudo-first-orde kinetics of the SMX degradation process was obtained by linear regression of ln [SMX]t to $[SMX]_0$ (Eq.(1)), and the pseudo-first-order rate constant (k_{obs}) was obtained [22].

$$-\ln\left(\frac{[SMX]_t}{[SMX]_0}\right) = K_{obs}t \quad (1)$$

$$\ln k_{obs} = \ln A - \frac{Ea}{RT} \quad (2)$$

Here, $[SMX]_0$ and $[SMX]_t$ were represented to initial and terminated concentration of SMX, k_{obs} , R and A are represent the rate constant, universal gas constant (8.314 J mol^{-1} K^{-1}) and pre-exponential factor [22].

3. Results and discussion

3.1 Morphology and structure analysis.

3.1.1 SEM Morphology. As shown in Fig. 1, pristine *g*-C3N5 exhibits a smooth blocky morphology (Fig. 1a), while *g*-C3N4 has a rough surface (Fig. 1b). The CN-AT homojunction shows a hierarchical structure with an irregular surface (Fig. 1c), attributed to the composite formation of C3N4 and C3N5. The rCN-AT sample displays a coral-rose-like porous structure (Fig. 1d), induced by the KBr template, which acts as a pore-forming agent to create a hierarchical porous network during calcination.

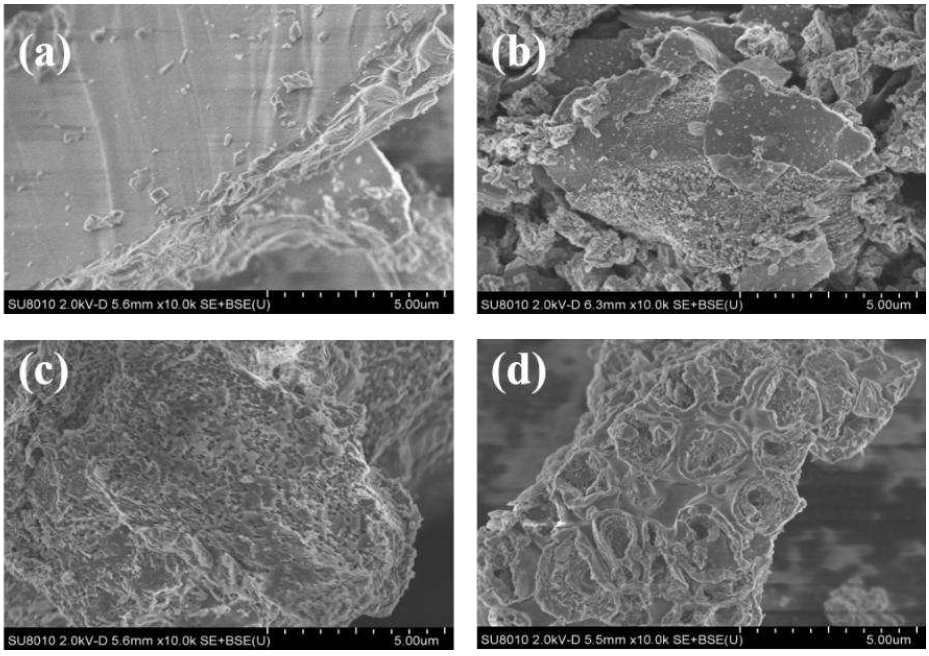


Fig.1 SEM image of C3N5 (a), C3N4 (b), CN-AT (c) and rCN-AT (d).

*3.1.2 BET Surface Area and Porosity***.** All samples exhibit typical IV N_2 adsorption-desorption isotherms, indicating mesoporous structures [33] (Fig. S1a). As shown in Table 1, the BET surface area (S_{BET}) of rCN-AT is 25.56 $m^2 \cdot g^{-1}$, which is higher than that of CN-AT (16.85 $m^2 \cdot g^{-1}$), C3N4 (9.23 $m^2 \cdot g^{-1}$), and C3N5 (1.92 $m^2 \cdot g^{-1}$). rCN-AT also has the largest pore volume (0.123 $cm^3 \cdot g^{-1}$) and pore size (17.63 nm). The enhanced porosity of rCN-AT provides abundant active sites for PMS adsorption and activation, facilitating mass transfer during the reaction.

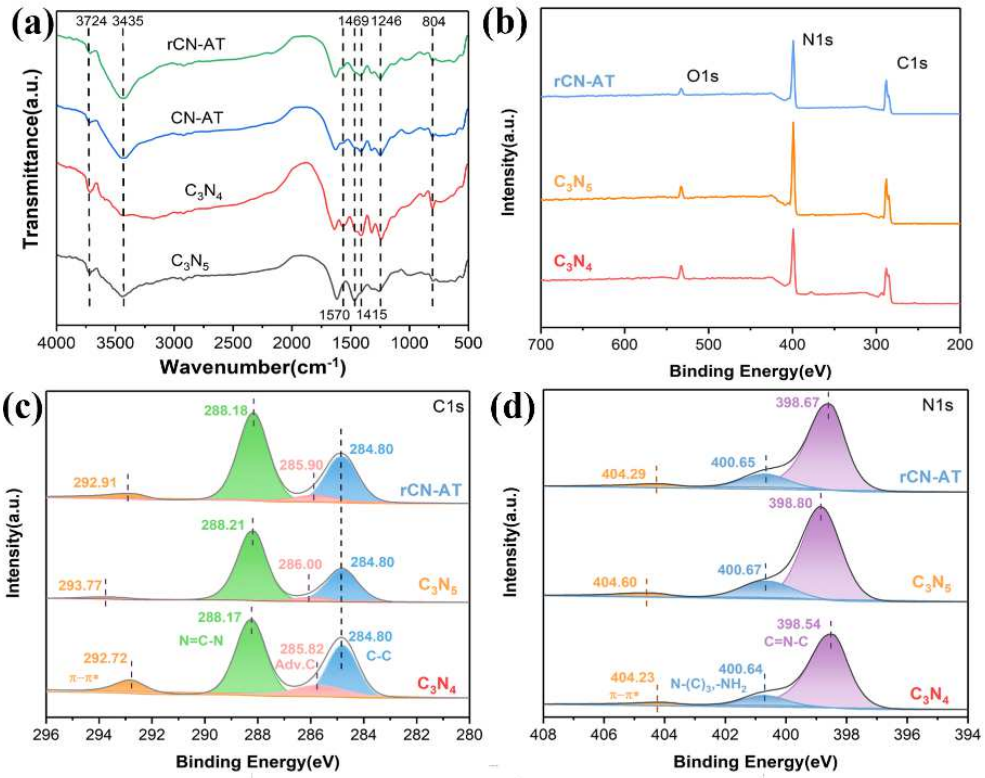
Table 1

Microstructural properties of the as-prepared samples

Sample	S_{BET} ($m^2 \cdot g^{-1}$)	Pore size (nm)	pore volume (cm^3 g^{-1})
C**3**N**5**	1.92	8.36	0.006
C**3**N**4**	9.23	8.66	0.019
CN-AT	16.85	11.37	0.042
rCN-AT	25.56	17.63	0.123

3.1.3 XRD and FTIR Analysis. The XRD patterns (Fig. S1b) show that C3N4 has a strong diffraction peak at 27.46° (corresponding to the (002) plane, interlayer stacking of aromatic rings) and a weak peak at 12.92° (corresponding to the (100) plane, in-plane triazine ring repetition) [37]. The (002) peak of C3N5 is broader and weaker than that of C3N4, indicating a denser structure (consistent with its small (S_{BET}) [34]. The CN-AT sample shows a (002) peak intensity between C3N4 and C3N5, confirming homojunction formation. The (002) peak of rCN-AT is further weakened, suggesting a more disordered and porous structure induced by KBr.

The FTIR spectra (Fig. 2a) show that C3N4 has a characteristic peak at 804 cm^{-1} (triazine ring bending vibration) [35] , while C3N5 exhibits strong absorption bands at 1200–1650 cm^{-1} (C-N stretching vibrations) and peaks at 3435 cm^{-1} (-OH from adsorbed water) and 3724 cm^{-1} (-NH_2 from uncondensed 3-amino-1,2,4-triazole) [36, 37]. The CN-AT and rCN-AT samples retain all typical peaks of C3N4 and C3N5, indicating that the chemical structure of the carbon nitrides is remains unchanged after homojunction formation.



141

142 **Fig.2** FTIR spectra (a), XPS survey spectra (b) and high resolution C1s (c) and N1s (d) of the as-prepared

143 samples

144 *3.1.4 XPS Analysis.* The C 1s XPS spectrum of C3N4 (Fig. 2c) shows peaks at 284.80 eV (adventitious carbon),

145 288.18 eV (N-C=N), and 292.91 eV (π-π* transitions) [38]. The N 1s spectrum (Fig. 2d) exhibits three peaks:

146 398.54 eV (C=N-C, N_2C), 400.64 eV (N-$(C)_3$ or -NH_2, N-$(C)_3$), and 404.23 eV (π-π* transitions) [39]. For C3N5 ,

147 the N 1s peak shifts to a higher binding energy, possibly due to the presence of N=N bonds [40]. The N/C ratio of

148 rCN-AT is between C3N4 (1.24) and C3N5 (1.53), indicating that the homojunction has been successfully

149 constructed. The rCN-AT sample has a C 1s and N 1s binding energy between C3N4 and C3N5, further confirming

150 homojunction formation. The N_{3C}/N_{2C} ratio of rCN-AT (0.16) is between C3N4 (0.12) and C3N5 (0.22),

151 indicating a strong interaction between C3N4 and C3N5 via an internal electric field—this promotes charge

152 transfer [41].

153 *3.2 Photoelectrochemical property*.

154 *3.2.1 UV-Vis DRS and PL.* The UV-Vis DRS (Fig. 3a) shows that *g*-C3N5 has two absorption edges at ~480 nm

155 and ~650 nm, corresponding to band-to-band transitions [42, 43]. The CN-AT sample has an absorption edge

156 between C3N4 and C3N5, extending the optical response range via homojunction formation. The rCN-AT sample

157 exhibits stronger visible-light absorption, attributed to its porous structure and enhanced π-π* conjugation [44].

158 The PL spectra (Fig. 3b) show that C3N4 and C3N5 have strong emission peaks at ~430 nm, corresponding to the

recombination of photogenerated electrons and holes in carbon nitrides. The PL peak intensity of CN-AT is lower than that of the pristine samples, and rCN-AT shows the lowest intensity—confirming that the homojunction and porous structure effectively inhibit charge recombination.

3.2.2 Photocurrent and EIS. The transient photocurrent response (Fig. 3c) shows that rCN-AT has the highest photocurrent intensity, followed by CN-AT, C3N4 and C3N5. This indicates that rCN-AT has the most efficient charge separation [32]. The photocurrent of the rCN-AT homojunction gradually decreases with the increase of illumination time, which may be caused by the charge carriers transfer to the surface [45]. Based on the above research, the built-in electric field in the rCN-AT homojunction can effectively promote photoexcited charge separation. The EIS Nyquist plots (Fig. 3d) show that rCN-AT has the smallest arc radius, indicating lower electron transfer resistance—this facilitates charge transport during PMS activation [31]. This is consistent with an increase in the photocurrent response intensity (Figure 4b) and a decrease in the peak PL intensity.

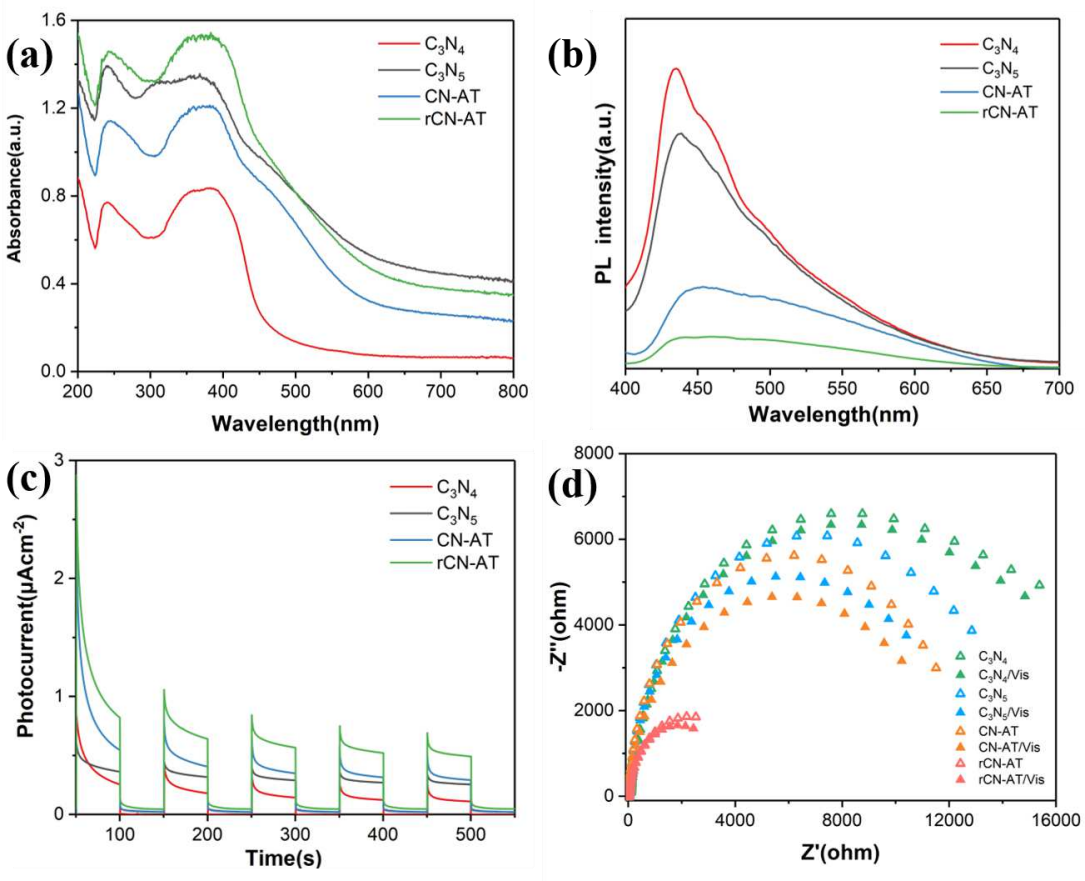


Fig. 3 UV-vis diffuse reflection spectra (a), photoluminescence (PL) spectra (b), transient photocurrent response (c), and EIS Nyquist plots (d) of the as-prepared samples

3.3 *PMS activation for SMX oxidation.*

3.3.1 *Catalytic Performance Comparison.* To assess the catalytic performance of rCN-AT (with

homojunction structure and enhanced specific surface area) in PMS activation for SMX degradation, comparative experiments were carried out using C3N4, C3N5, and CN-AT as reference catalysts. The experiments were conducted under three reaction systems: PMS only, visible light only and catalyst/PMS/Vis (C3N4/PMS/Vis, *g*-C3N5/PMS/Vis, CN-AT/PMS/Vis, and rCN-AT/PMS/Vis). As shown in Fig. S2a, after 45 min of reaction, the SMX degradation rates of the C3N4/PMS/Vis, C3N5/PMS/Vis, CN-AT/PMS/Vis, and rCN-AT/PMS/Vis systems are 28.85%, 33.92%, 83.64%, and 99.98%, respectively. The rCN-AT system also has the highest reaction rate constant (k_{obs} = 0.123 min^{-1}), which is 12.2 times higher than g-C3N4 (k_{obs} = 0.0101 min^{-1}) and 8.8 times higher than g-C3N5 (k_{obs} = 0.0140 min^{-1}) (Fig. S2b). Clearly, the rCN-AT/PMS/Vis system exhibits the best SMX degradation performance. Control experiments (Fig. 4a) show that rCN-AT adsorption, PMS only, visible light only, rCN-AT/Vis, and rCN-AT/PMS achieve only 0.74%, 16.54%, 22.94%, 20.16%, and 56.87% SMX degradation, respectively. This confirms the synergistic effect of rCN-AT, PMS, and visible light in promoting SMX degradation.

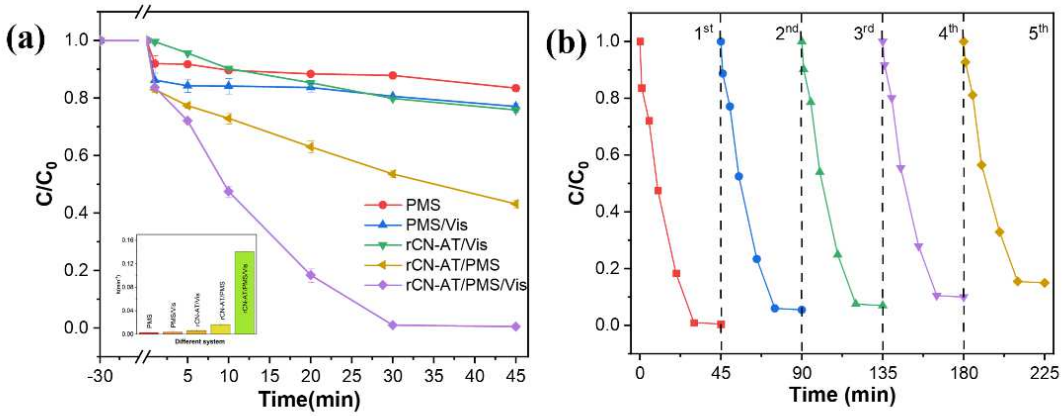


Fig. 4 Degradation of SMX in rCN-AT under different conditions (a), Recycling experiments of SMX degradation in suspensions of rCN-AT (b).

3.3.2 Catalyst Stability. The reusability test (Fig.4b) shows that after five cycles, the SMX degradation rate of rCN-AT remains at ~85%, which is still higher than the initial performance of C3N4 and C3N5. The slight activity decrease may be due to intermediate product adsorption on active sites. These results demonstrate that rCN-AT has strong stability, good economic benefits, and practical application potential.

3.3.3 Influence factors on SMX degradation.

Initial pH. Solution pH is a critical factor affecting PMS activation and contaminant degradation, as it influences the speciation of PMS, catalyst surface charge, and reactive species generation [3]. The rCN-AT/PMS/Vis system

exhibits high SMX degradation efficiency over a wide pH range (3.16–9.09) (Fig. 5a,b). Previous reports have shown that deprotonated SMX has higher reactivity than protonated SMX [22]. The optimal pH is near neutral (pH 7.07, 99.02% within 30 min), which aligns with the pKa values of SMX (pKa_1 = 1.8, pKa_2 = 5.6) and PMS (pKa = 9.4) [3]. At pH < pKa_2 of SMX, SMX exists as a neutral molecule, while PMS is primarily in the form of HSO_5^-. The neutral surface of rCN-AT (isoelectric point ~3.9, Fig. 5a) facilitates adsorption of both neutral SMX and HSO_5^-, promoting their interaction [22]. At alkaline pH (pH > 9.4), PMS dissociates into SO_5^{2-}, which has lower reactivity than HSO_5^-, leading to reduced activation efficiency. Additionally, high pH may induce self-decomposition of PMS, further decreasing degradation performance [46].

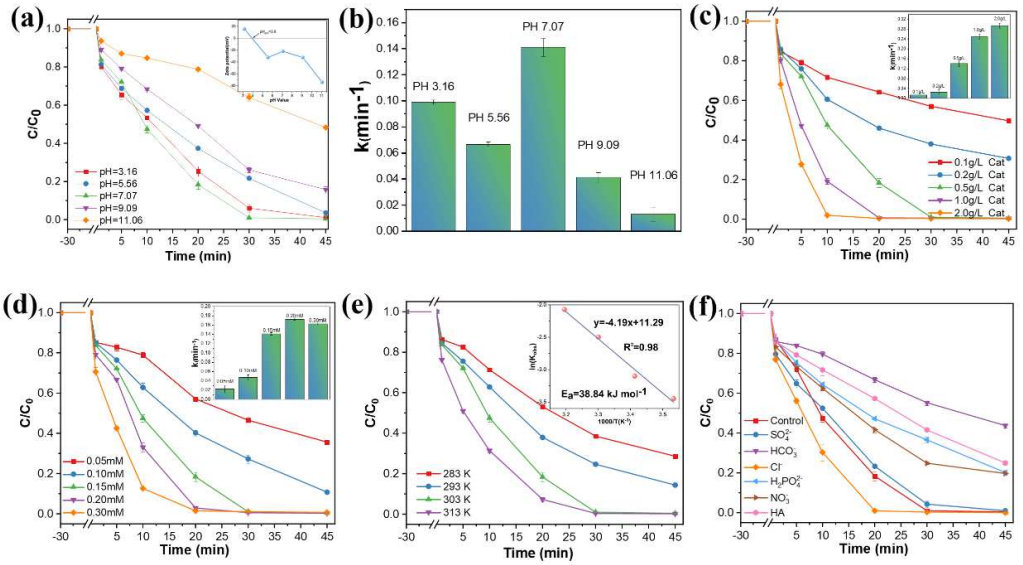


Fig. 5 Effect of initial pH (a and b), dosage of PMS (c), dosage of photocatalyst (d), temperatures (e) and different inorganic anions and humic acids (HA) (f) on SMX degradation in rCN-AT/PMS/Vis system.

Catalyst Dosage. The influence of rCN-AT dosage (0.1–2.0 g·L⁻¹) on SMX degradation is presented in Fig. 5c. As the dosage increases from 0.1 to 1.0 g·L⁻¹, SMX degradation efficiency rises from 62.4% to 99.98%, and the k_{obs} increases from 0.028 to 0.123 min⁻¹. This is because higher catalyst dosage provides more active sites for PMS adsorption and activation. However, when the dosage exceeds 1.0 g·L⁻¹, the degradation efficiency slightly decreases (to 95.3% at 2.0 g·L⁻¹). Excessive catalyst particles may cause light scattering, visible-light utilization efficiency reducing, and leading to mutual aggregation of active sites, which hinders charge transfer[47].

PMS dosage. As shown in Figure 5d, SMX degradation efficiency increases with PMS dosage from 0.05 to 0.2 mM: 78.6% (0.05 mM), 99.98% (0.2 mM), and 98.2% (0.3 mM). The k_{obs} reaches a maximum of 0.123 min⁻¹ at 0.2 mM PMS. Sufficient PMS provides more oxidizing species, but excessive PMS may act as a scavenger for

reactive radicals ($HSO_5^- + SO_4^{\cdot-} \rightarrow SO_4^{2-} + SO_5^{\cdot-} + H^+$), reducing the effective concentration of reactive species[48].

Temperature. Temperature affects the reaction rate by influencing molecular diffusion and activation energy [49]. Increasing temperature from 283 K to 313K enhances SMX degradation (Fig. 5e), with an activation energy (Ea) of 38.84 kJ·mol^{-1} (inset of Fig. 5e). This value is higher than diffusion-controlled reactions (10~13 kJ·mol^{-1}) [22], indicating that the reaction is dominated by surface chemical reactions. From the K_{obs} of SMX degradation during the oxidation of rCN-AT /PMS/Vis, on the catalyst surface the inherent chemical reaction rate was the dominant factor rather than the mass transfer rate [50]. In addition, for the out-sphere interactions are usually diffusion-controlled reactions, the rCN-AT /PMS/Vis reaction system was most likely to be an intra-sphere electron transfer process.

Coexisting Anions. Natural water contains various anions that may affect AOPs performance. Therefore, we particularly investigated the influence of inorganic ions and humic acid on the removal of SMX (Fig.5f). Coexisting anions show different effects: HCO_3^-, $H_2PO_4^{2-}$, NO_3^-, inhibit SMX degradation (order: HCO_3^-> $H_2PO_4^{2-}$>NO_3^-) by quenching $SO_4^{\cdot-}$ and •OH (Eq.3) [51, 52], while Cl^- promotes degradation by generating reactive chlorine species (e.g., HOCl, Cl_2, and$Cl\cdot$) via reactions with PMS and $SO_4^{\cdot-}$ (Eq.4-7) [31, 51, 53].

$$HSO_5^- + HCO_3^- \rightarrow HCO_4^- + HSO_4^- \quad (3)$$

$$Cl^- + HSO_5^- \rightarrow SO_4^{2-} + HOCl \quad (4)$$

$$2Cl^- + H^+ + HSO_5^- \rightarrow SO_4^{2-} + Cl_2 + H_2O \quad (5)$$

$$Cl^- + SO_4\cdot^- \rightarrow SO_4^{2-} + Cl\cdot \quad (6)$$

$$Cl^- + Cl\cdot \rightarrow Cl_2\cdot^- \quad (7)$$

Additionally, the degradation of SMX is significantly inhibited by the existence of HA. As reported, natural organic matters (NOMs) typically act as free radical scavengers in advanced oxidation processes (AOPs) by competing with reactive oxygen species (ROS), reducing the decomposition efficiency of target contaminants [51, 52]. Specifically, phenolic moieties in NOMs can inhibit the photochemical conversion of aniline compounds in sulfamethoxazole (SMX) via the excited triplet state; their reduction of SMX radical cations may also hinder SMX removal. Additionally, humic acid (HA) competes for active sites on the catalyst surface, and its spatial and electrostatic effects further block peroxymonosulfate (PMS) from reaching the catalyst surface, thus inhibiting SMX degradation .

3.4 Degradation mechanism analysis.

3.4.1 Reactive Species Identification. Quenching tests and EPR analysis revealed the involvement of $\cdot SO_4^{\cdot-}$, $\cdot OH$, $\cdot O_2^-$, $^1O_2$ and h^+ in the degradation process, with $\cdot O_2^-$, $^1O_2$ and h^+ identified as the dominant reactive species. As shown in Fig. S3, the SMX degradation efficiency decreases slightly (to 89.2%) with the addition of TBA, indicating a minor contribution of $\cdot OH$. When MeOH is added, the degradation efficiency drops to 72.5%, suggesting that $\cdot SO_4^{\cdot-}$ plays a more important role than $\cdot OH$ but is not the dominant species. The SMX degradation rate shows a decrease from 0.0064 min^{-1}, 0.0103min^{-1} or 0.005min^{-1} along with adding p-BQ, EDTA-2Na or FFA. These confirm that h^+, $\cdot O_2^-$, $^1O_2$ are the dominant reactive species in the rCN-AT/PMS/Vis system.

EPR spectra confirm that $DMPO-\cdot O_2^-$ (1:1:1:1 quartet) and TEMPO-h^+ are clearly observed in Fig.6a,b. While signals of DMPO-$\cdot SO_4^{\cdot-}$ (1:1:1:1:1:1 sextet and DMPO-$\cdot OH$ (1:2:2:1 quartet) are weaker in the rCN-AT/PMS/Vis system. For $^1O_2$ detection (Fig.6d), the characteristic triplet signal of TMP-$^1O_2$ is observed, confirming $^1O_2$ generation via PMS activation.

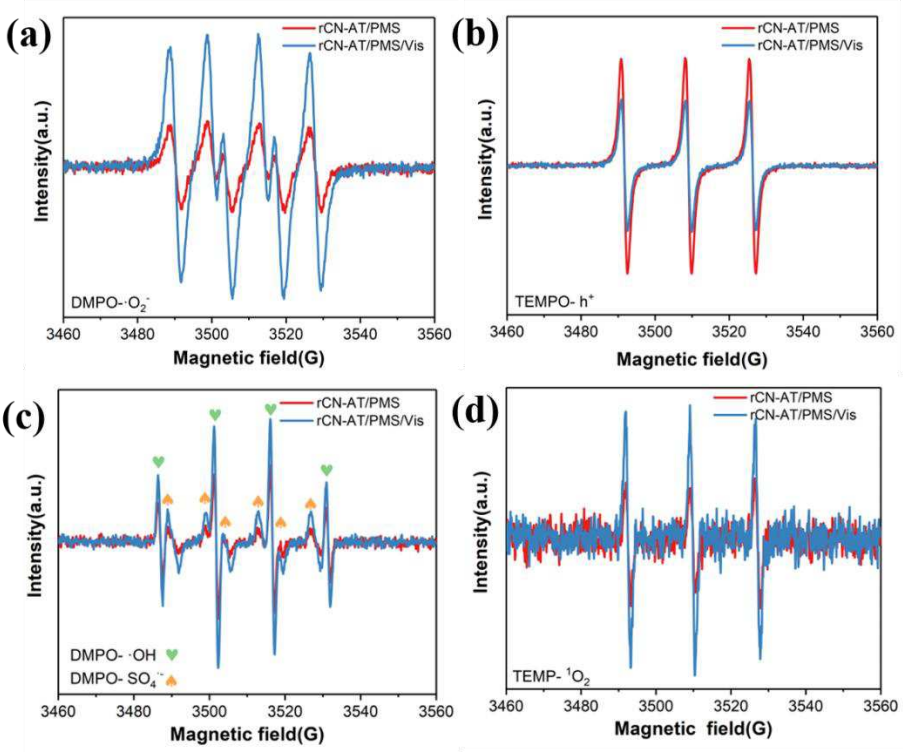


Fig.6 ESR spectra of CN-AT under dark and visible light irradiation, DMPO-DMSO-$\cdot O_2^-$ (a), TEMPO-h^+ (b), DMPO- $SO_4^{\cdot-}$/$\cdot OH$ (c), TEMP-$^1O_2$ (d)

According to the ESR results (Fig. 6), signals corresponding to reactive species were detected in both the PMS-only system and the visible light-PMS coexistence system. For the rCN-AT/PMS system, distinct ESR signals of reactive species were observed, indicating that rCN-AT can activate PMS even under dark conditions to generate reactive radicals including $SO_4^{\cdot-}$, $\cdot OH$, $\cdot O_2^-$ and $^1O_2$. This result may be attributed to the involvement of electron-

deficient carbon atoms in the homojunction structure in PMS activation. When visible light was presented in the rCN-AT/PMS system, the intensity of reactive species signals was significantly enhanced, demonstrating that the photocatalytic process promotes the formation of reactive species. Specifically, the signals of TEMPO-h^+, DMSO-$\cdot O_2^-$ and TEMP-$^1O_2$ were stronger than the DMPO-·OH, while the DMPO- $SO_4^{\cdot-}$ signal was relatively weak. These results further confirm that h^+, $\cdot O_2^-$, $^1O_2$ are the dominant reactive species.

3.4.2 Electronic band structure determination. Based on DRS results, Tauc plot method was employed to convert the diffuse reflection data [27, 54]. According to Fig 7 the band gap width (Eg) of C_3N_4 and C_3N_5 were determined to be 2.80eV and 2.00eV, respectively. Using Mott-Schottky plots (Fig. 7a, b) and the conversion equations:$E_{Ag/AgCl} = E_{RHE} - 0.059\ pH - 0.197$ and $E_{NHE} = E_{RHE} - 0.059\ pH$ [55], the conduction band (CB) potentials of C_3N_4 and C_3N_5 were calculated to be approximately -1.185 and -1.598 V (at pH= 5.95 vs. Ag/AgCl), respectively. The valence band (VB) potentials are set as 1.75 V (for g-C3N4) and 0.54 V (for g-C3N5) using $E_{VB} = E_{CB} + E_g$. Under light irradiation, both C_3N_4 and C_3N_5 can generate photogenerated electron-hole pairs. In the rCN-AT homojunction, C_3N_4 possesses a less negative CB potential compared to C_3N_5, driving the photogenerated electrons transferred from the CB of C_3N_5 to C_3N_4. Meanwhile, since C_3N_5 has a higher VB potential than C_3N_4 in the rCN-AT homojunction, photogenerated holes migrate from the VB of C_3N_4 to the VB of C_3N_5.

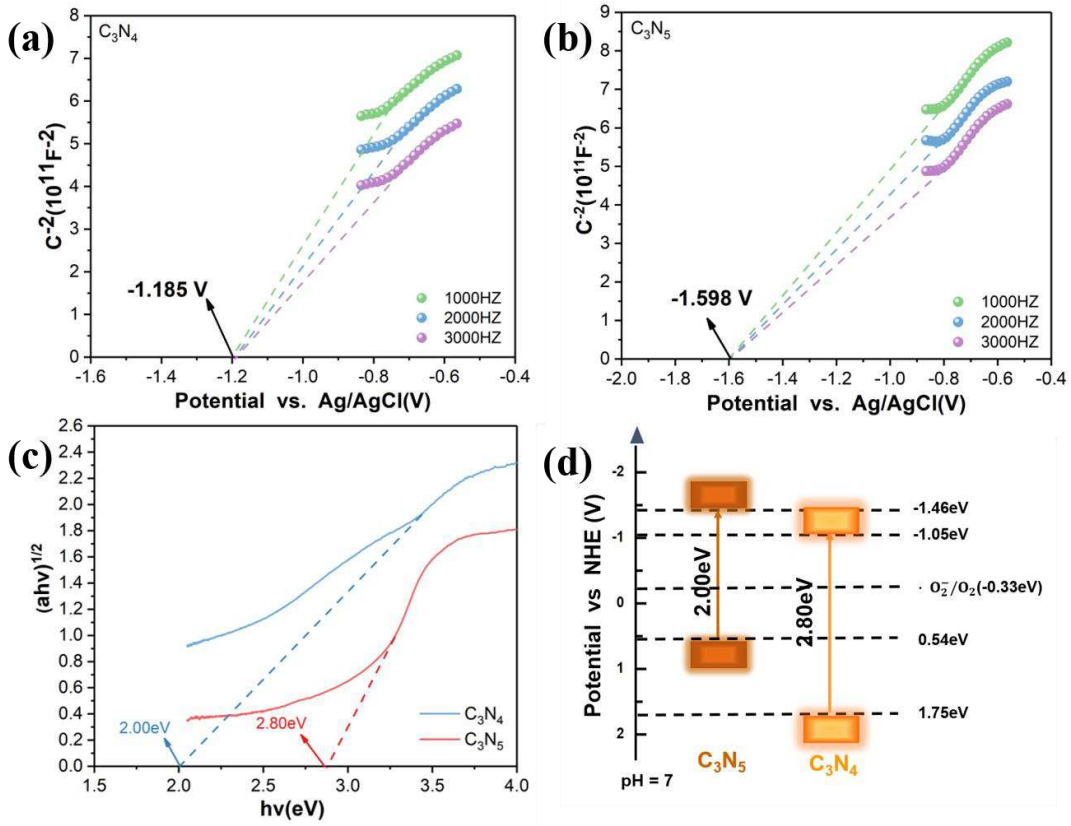


Fig.7 Mot-Schottky plots (a and b), Tauc plot (c) and the calculated band diagram (d) of C_3N_4 and C_3N_5 samples

Linear sweep voltammetry (LSV) curves were measured to verify PMS's role in the photocatalytic process [21, 22, 31, 32]. As shown in Fig. S4, the current response of rCN-AT in the dark was lower than with light irradiation. Notably, the current intensity of rCN-AT was significantly enhanced in both irradiation and dark conditions, introducing PMS. This result indicates that as an efficient electron acceptor, PMS can improve the transfer efficiency of photogenerated electrons.

A plausible reaction mechanism was proposed sulfamethoxazole (SMX) degradation mediated by peroxymonosulfate (PMS) activated by the C3N4/C3N5 homojunction (rCN-AT). Within the rCN-AT/PMS/Vis system, two core processes (photocatalysis and PMS activation) operate in a synergistic manner to drive SMX degradation. Upon irradiation with visible light, the rCN-AT homojunction undergoes photoexcitation, resulting in the generation of photogenerated electrons (e^-) and holes (h^+). Specifically, the h^+ localized in the valence band (VB) of C3N4 migrate to C3N5, whereas the photogenerated e^- in the conduction band (CB) of C3N5 transfer to the CB of C3N4. The migrated h^+ are capable of reacting with PMS molecules adsorbed on the surface of C3N5. Meanwhile, the asymmetric structure of PMS ($HO\text{-}O\text{-}SO_3^-$) enables it to accept photogenerated e^- from the CB of C3N4.

The integrated process of photocatalysis and PMS activation achieves two key goals via strong synergy: (i) PMS significantly promotes the separation and transfer of photogenerated electrons (e^-) and and holes (h^+) in rCN-AT; (ii) PMS gets activated upon accepting photogenerated e^-, yielding reactive species. As outlined in the schematic (Fig.8), visible light excitation of rCN-AT generates photogenerated e^-(CB) and h^+(VB) (Eq. (8)). Given that the potentials of $\cdot OH/OH^-$ (2.38 V vs. NHE) and $\cdot OH/H_2O$ (2.72 V vs. NHE) are more positive than rCN-AT's VB potential rCN-AT (0.31 V vs. NHE) [31], h^+(VB) cannot react with OH^-/H_2O. Instead, it reacts with HSO_5^- to form $SO_5\cdot^-$ (Eq. (9)). Combined with earlier radical quenching results, h^+(VB) primarily acts to directly degrade SMX.

Moreover, e^-(CB) is engaged in two reactions: (i) reacting with dissolved oxygen to generate $\cdot O_2^-$ (Eq. (10)), this is because the potential of as the potential of $O_2/\cdot O_2^-$ (-0.33 V vs. NHE) is less negative than the rCN-AT's CB potential (-1.58 V vs. NHE) [32]; (ii) activating PMS (HSO_5^-) to generate $SO_4\cdot^-$ (Eq. (11)). Other possible reactions in the rCN-AT/PMS/Vis system include the conversion of $SO_4\cdot^-$ to $\cdot OH$ via reactions with H_2O or OH^- (Eqs. (12) and (13)). Additionally, quenching experiments and EPR analysis confirm that non-radical pathways contribute to SMX degradation. The generated $SO_5\cdot^-$ can further react to form $^1O_2$ (Eq. (14)). Ultimately, the rCN-AT/PMS/Vis system produces h^+, $\cdot O_2^-$, $SO_4\cdot^-$, $^1O_2$, and $\cdot OH$ as reactive species for efficient SMX degradation (Eq. (15)).

$$\mathrm{rCN-AT} + \mathrm{Vis} \rightarrow \mathrm{e^-(CB)} + \mathrm{h^+(VB)} \quad (8)$$

$$HSO_5^- + h^+(VB) \rightarrow SO_5^{\cdot-} + H^+ \quad (9)$$

$$e^-(CB) + O_2 \rightarrow \cdot O_2^- \quad (10)$$

$$HSO_5^- + e^-(CB) \rightarrow SO_4^{\cdot-} + OH^- \quad (11)$$

$$SO_4^{\cdot-} + H_2O \rightarrow SO_4^{2-} + \cdot OH + H^+ \quad (12)$$

$$SO_4^{\cdot-} + OH^- \rightarrow SO_4^{2-} + \cdot OH \quad (13)$$

$$2SO_5^{\cdot-} + H^+ \rightarrow 2SO_4^{\cdot-} + {}^1O_2 \quad (14)$$

$${}^1O_2 + h^+ + \cdot OH + SO_4^{\cdot-} + SMX \rightarrow 降解产物 \quad (15)$$

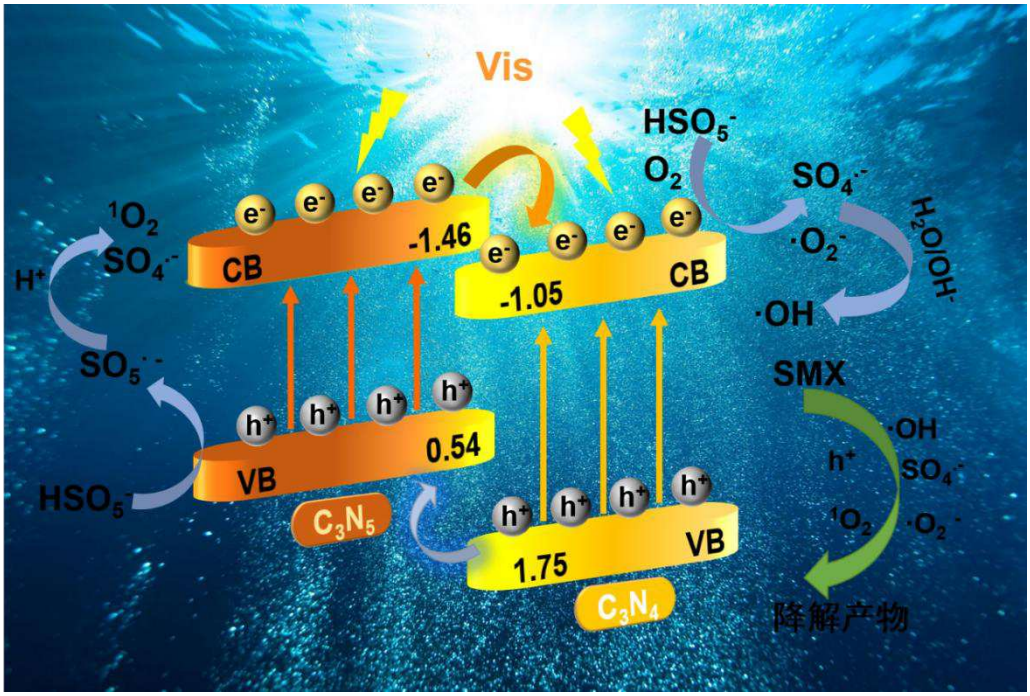


Fig.8 Proposed degradation mechanism of SMX by the rCN-AT/PMS/Vis system

4. Conclusions

In summary, a novel metal-free g-C3N4/g-C3N5 homojunction (rCN-AT) was successfully synthesized via a KBr-assisted thermal polymerization method. The rCN-AT/PMS/Vis system exhibited the highest and most stable SMX degradation efficiency among all tested systems, achieving ~99.98% SMX removal within 45 min—far exceeding the performance of g-C3N4/PMS/Vis (28.85%), g-C3N5/PMS/Vis (33.92%), and CN-AT/PMS/Vis (83.64%).

The enhanced catalytic performance of rCN-AT is attributed to its unique homojunction interface and large specific surface area (25.56 $m^2 \cdot g^{-1}$), which facilitate efficient interfacial charge transfer and promote effective PMS activation.

Furthermore, quenching experiments and spectroscopic analysis confirmed the involvement of five reactive species $\cdot SO_4^-$, $\cdot OH$, $\cdot O_2^-$, $^1O_2$ and h^+, with h^+, $\cdot O_2^-$, and $^1O_2$ identified as the dominant contributors. Evidence of electron transfer between PMS and rCN-AT suggests that SMX degradation proceeds via both radical and non-radical pathways.

This study provides a new strategy for designing metal-free homojunction catalysts for PMS activation and offers insights into efficient antibiotic degradation in water treatment.

Acknowledgments

This study was supported by the Specialized Research on Comprehensive Lake Management: Key Technologies for Three-Dimensional Intelligent Tracking of Lake Morphology and Habitat Development (HBSLKY202402), Major Scientific Research Project of Water Conservancy in Hubei Province (420000-2023-09011), and financially supported by Hubei Provincial Natural Science Foundation of China (2023AFB788), Fundamental Research Funds for the Central Universities: South-Central MinZu University (Nos. PTZ25016).

Statements and Declarations

The authors declare that they have no known competing financial interests or personal relationships that could have appeared to influence the work reported in this paper.

References

[1] H. Ren, R. Wang, L. Ying, E. Iyobosa, G. Chen, D. Zang, M. Tong, E. Li, R. Nerenberg, Removal of sulfamethoxazole in an algal-bacterial membrane aerated biofilm reactor: Microbial responses and antibiotic resistance genes, Water Research, 268 (2025).

[2] K. Shang, R. Morent, N. De Geyter, Y. Wang, Z. Yang, Plasma catalytic degradation of sulfamethoxazole in water with Fe/Mn-LDO catalyst: Performance and mechanism, Separation and Purification Technology, 360 (2025).

[3] J. Yan, J. Li, J. Peng, H. Zhang, Y. Zhang, B. Lai, Efficient degradation of sulfamethoxazole by the CuO@Al2O3 (EPC) coupled PMS system: Optimization, degradation pathways and toxicity evaluation, Chemical Engineering Journal, 359 (2019) 1097-1110.

[4] G. Lu, X. Yang, Z. Li, H. Zhao, C. Wang, Contamination by metals and pharmaceuticals in northern Taihu Lake (China) and its relation to integrated biomarker response in fish, Ecotoxicology, 22 (2013) 50-59.

[5] T.B. Minh, H.W. Leung, I.H. Loi, W.H. Chan, M.K. So, J.Q. Mao, D. Choi, J.C.W. Lam, G. Zheng, M. Martin, J.H.W. Lee, P.K.S. Lam, B.J. Richardson, Antibiotics in the Hong Kong metropolitan area: Ubiquitous distribution and fate in Victoria Harbour, Marine Pollution Bulletin, 58 (2009) 1052-1062.

[6] D. Hu, H. Min, H. Wang, Y. Zhao, Y. Cui, P. Wu, H. Ge, K. Luo, L. Zhang, W. Liu, A. Wang, Performance of an up-flow anaerobic bio-electrochemical system (UBES) for treating sulfamethoxazole (SMX) antibiotic wastewater, Bioresource Technology, 305 (2020) 123070.

[7] J. Du, W. Guo, H. Wang, R. Yin, H. Zheng, X. Feng, D. Che, N. Ren, Hydroxyl radical dominated degradation of aquatic sulfamethoxazole by Fe0/bisulfite/O2: Kinetics, mechanisms, and pathways, Water Research, 138 (2018) 323-332.

[8] L. Sui, H. Guo, Y.-Y. Yang, Z.-T. Dong, Q. Wu, C. Yi, C.-G. Niu, M. Yan, J.-J. Wang, L.-S. Feng, D.-W. Huang, Surface electric fields-enhanced biochar: A dual-action adsorbent and PMS activator for sulfamethoxazole removal, Separation and Purification Technology, 358 (2025).

[9] F. Ghanbari, M. Moradi, Application of peroxymonosulfate and its activation methods for degradation of environmental organic pollutants: Review %J Chemical Engineering Journal, Chemical Engineering Journal, 310 (2016).

[10] S. Yang, P. Wang, X. Yang, L. Shan, W. Zhang, X. Shao, R. Niu, Degradation efficiencies of azo dye Acid Orange 7 by the interaction of heat, UV and anions with common oxidants: Persulfate, peroxymonosulfate and hydrogen peroxide, Journal of Hazardous Materials, 179 (2010) 552-558.

[11] C. Qi, X. Liu, J. Ma, C. Lin, X. Li, H. Zhang, Activation of peroxymonosulfate by base: Implications for the degradation of organic pollutants, Chemosphere, 151 (2016) 280-288.

[12] W.-D. Oh, Z. Dong, T.-T. Lim, Generation of sulfate radical through heterogeneous catalysis for organic contaminants removal: Current development, challenges and prospects, Applied Catalysis B: Environmental, 194 (2016) 169-201.

[13] X. Liu, T. Zhang, Y. Zhou, L. Fang, Y. Shao, Degradation of atenolol by UV/peroxymonosulfate: Kinetics, effect of operational parameters and mechanism, Chemosphere, 93 (2013) 2717-2724.

[14] S. Su, W. Guo, C. Yi, Y. Leng, Z. Ma, Degradation of amoxicillin in aqueous solution using sulphate radicals under ultrasound irradiation, Ultrasonics Sonochemistry, 19 (2012) 469-474.

[15] Y. Gao, S. Li, Y. Li, L. Yao, H. Zhang, Accelerated photocatalytic degradation of organic pollutant over metal-organic framework MIL-53(Fe) under visible LED light mediated by persulfate, Applied Catalysis B:

Environmental, 202 (2017) 165-174.
[16] Y. Jia, L. Duan, H. Li, C. Zhang, Q. Gao, H. Zhang, S. Li, M. Li, Visible light activation of persulfate by α-Fe2O3/PDINH photocatalyst for sulfamethoxazole degradation, Separation and Purification Technology, 354 (2025).
[17] X. Yang, X. Ma, H. Yang, J. Zhao, Y. Tang, P. Ning, C. Wang, G. Zhang, S. Bao, K. Li, Piezoelectric polarization-induced electric field in Co-Co2P/BNT composite for enhanced peroxymonosulfate activation and rapid degradation of sulfamethoxazole, Journal of Environmental Chemical Engineering, 13 (2025).
[18] L. Tang, X. Lei, C. Zou, J. Li, J. Liu, B. Liu, C. Wang, J. Liang, Monoethanolamine modulated Cu(II)/PMS system for sulfamethoxazole degradation: The role of Cu(II)-OOSO3- metastable complex and rapid copper species cycling, Chemical Engineering Journal, 512 (2025).
[19] Y. Zhang, Y. Liu, Y. Li, H. Cheng, C. Zhu, Y. Shen, S. Shao, J. Xue, D. Zhou, F. Cao, Cost-effective micro/mesoporous biochar derived from soda residue-assisted hydrocarbonization and activation of crop waste for sulfamethoxazole removal from water environments, Bioresource Technology, 437 (2025).
[20] W.-S. Chen, C.-P. Huang, Mineralization of aniline in aqueous solution by electrochemical activation of persulfate, Chemosphere, 125 (2015) 175-181.
[21] J. Zhang, X. Zhao, Y. Wang, Y. Gong, D. Cao, M. Qiao, Peroxymonosulfate-enhanced visible light photocatalytic degradation of bisphenol A by perylene imide-modified g-C3N4, Applied Catalysis B: Environmental, 237 (2018) 976-985.
[22] Y. Li, J. Li, Y. Pan, Z. Xiong, G. Yao, R. Xie, B. Lai, Peroxymonosulfate activation on FeCo2S4 modified g-C3N4 (FeCo2S4-CN): Mechanism of singlet oxygen evolution for nonradical efficient degradation of sulfamethoxazole, Chemical Engineering Journal, 384 (2020) 123361.
[23] J. Yan, H. Wu, H. Chen, Y. Zhang, F. Zhang, S.F. Liu, Fabrication of TiO2/C3N4 heterostructure for enhanced photocatalytic Z-scheme overall water splitting, Applied Catalysis B: Environmental, 191 (2016) 130-137.
[24] Y. Li, C. Zhang, G. Zhao, Z. Zhang, P. Su, Y. Li, Y. Mu, W. Zhou, A critical review on the activation of peroxymonosulfate by MOFs for antibiotics degradation: Affecting factor, performance and mechanism, Journal of Environmental Chemical Engineering, 12 (2024).
[25] G. Manickavasagam, C. He, K.-Y.A. Lin, M. Saaid, W.-D. Oh, Recent advances in catalyst design, performance, and challenges of metal-heteroatom-co-doped biochar as peroxymonosulfate activator for environmental remediation, Environmental research, 252 (2024).
[26] P. Kumar, E. Vahidzadeh, U.K. Thakur, P. Kar, K.M. Alam, A. Goswami, N. Mahdi, K. Cui, G.M. Bernard, V.K. Michaelis, K. Shankar, C3N5: A Low Bandgap Semiconductor Containing an Azo-Linked Carbon Nitride Framework for Photocatalytic, Photovoltaic and Adsorbent Applications, Journal of the American Chemical Society, 141 (2019) 5415-5436.
[27] H. Wang, M. Li, H. Li, Q. Lu, Y. Zhang, S. Yao, Porous graphitic carbon nitride with controllable nitrogen vacancies: As promising catalyst for enhanced degradation of pollutant under visible light, Materials & Design, 162 (2019) 210-218.
[28] J. Zhang, Z. Ma, Porous g-C3N4 with enhanced adsorption and visible-light photocatalytic performance for removing aqueous dyes and tetracycline hydrochloride, Chinese Journal of Chemical Engineering, 26 (2018) 753-760.
[29] X. Li, Z. Ao, J. Liu, H. Sun, A.I. Rykov, J. Wang, Topotactic Transformation of Metal–Organic Frameworks to Graphene-Encapsulated Transition-Metal Nitrides as Efficient Fenton-like Catalysts, ACS Nano, 10 (2016) 11532-11540.
[30] J. Zhang, B. Jing, Z. Tang, Z. Ao, D. Xia, M. Zhu, S. Wang, Experimental and DFT insights into the visible-

light driving metal-free C3N5 activated persulfate system for efficient water purification, Applied Catalysis B: Environmental, 289 (2021) 120023.
[31] Y. Wang, X. Zhao, D. Cao, Y. Wang, Y. Zhu, Peroxymonosulfate enhanced visible light photocatalytic degradation bisphenol A by single-atom dispersed Ag mesoporous g-C3N4 hybrid, Applied Catalysis B: Environmental, 211 (2017) 79-88.
[32] Z. Yin, M. Han, Z. Hu, L. Feng, Y. Liu, Z. Du, L. Zhang, Peroxymonosulfate enhancing visible light photocatalytic degradation of bezafibrate by Pd/g-C3N4 catalysts: The role of sulfate radicals and hydroxyl radicals, Chemical Engineering Journal, 390 (2020) 124532.
[33] H. Wang, M. Li, Q. Lu, Y. Cen, Y. Zhang, S. Yao, A Mesoporous Rod-like g-C3N5 Synthesized by Salt-Guided Strategy: As a Superior Photocatalyst for Degradation of Organic Pollutant, ACS Sustainable Chemistry & Engineering, 7 (2019) 625-631.
[34] C. Peng, L. Han, J. Huang, S. Wang, X. Zhang, H. Chen, Comprehensive investigation on robust photocatalytic hydrogen production over C3N5, Chinese Journal of Catalysis, 43 (2022) 410-420.
[35] X.J. She, L. Liu, H.Y. Ji, Z. Mo, Y.P. Li, L.Y. Huang, D.L. Du, H. Xu, H.M. Li, Template-free synthesis of 2D porous ultrathin nonmetal-doped g-C_3N_4 nanosheets with highly efficient photocatalytic H_2 evolution from water under visible light, Appl. Catal. B: Environ., 187 (2016) 144-153.
[36] E.I. García-López, Z. Abbasi, F. Di Franco, M. Santamaria, G. Marcì, L. Palmisano, Selective oxidation of aromatic alcohols in the presence of C3N4 photocatalysts derived from the polycondensation of melamine, cyanuric and barbituric acids, Research on Chemical Intermediates, 47 (2021) 131-156.
[37] C. Hu, Y.-H. Lin, M. Yoshida, S. Ashimura, Influence of Phosphorus Doping on Triazole-Based g-C3N5 Nanosheets for Enhanced Photoelectrochemical and Photocatalytic Performance, ACS Applied Materials & Interfaces, 13 (2021) 24907-24915.
[38] H. Wang, W. Guo, B. Liu, Q. Wu, H. Luo, Q. Zhao, Q. Si, F. Sseguya, N. Ren, Edge-nitrogenated biochar for efficient peroxydisulfate activation: An electron transfer mechanism, Water Research, 160 (2019) 405-414.
[39] X. She, H. Xu, Y. Xu, J. Yan, J. Xia, L. Xu, Y. Song, Y. Jiang, Q. Zhang, H. Li, Exfoliated graphene-like carbon nitride in organic solvents: enhanced photocatalytic activity and highly selective and sensitive sensor for the detection of trace amounts of Cu2+, Journal of Materials Chemistry A, 2 (2014) 2563-2570.
[40] G.P. Mane, S.N. Talapaneni, K.S. Lakhi, H. Ilbeygi, U. Ravon, K. Al-Bahily, T. Mori, D.-H. Park, A. Vinu, Highly Ordered Nitrogen-Rich Mesoporous Carbon Nitrides and Their Superior Performance for Sensing and Photocatalytic Hydrogen Generation, Angew. Chem. Int. Ed., 56 (2017) 8481-8485.
[41] H. Dong, X. Zhang, J. Li, P. Zhou, S. Yu, N. Song, C. Liu, G. Che, C. Li, Construction of morphology-controlled nonmetal 2D/3D homojunction towards enhancing photocatalytic activity and mechanism insight, Applied Catalysis B: Environmental, 263 (2020) 118270.
[42] X. He, D. Zhu, In situ solvothermal method of C3N5@NH2-MIL-125 composites with enhanced visible-light photocatalytic performance, Journal of Materials Science: Materials in Electronics, 33 (2022) 388-398.
[43] J. Zhang, H. Tao, S. Wu, J. Yang, M. Zhu, Enhanced durability of nitric oxide removal on TiO2 (P25) under visible light: Enabled by the direct Z-scheme mechanism and enhanced structure defects through coupling with C3N5, Applied Catalysis B: Environmental, 296 (2021) 120372.
[44] S. An, G. Zhang, K. Li, Z. Huang, X. Wang, Y. Guo, J. Hou, C. Song, X. Guo, Self-Supporting 3D Carbon Nitride with Tunable n → π * Electronic Transition for Enhanced Solar Hydrogen Production, Advanced Materials, 33 (2021) 2104361.
[45] Q. Gao, J. Xu, Z. Wang, Y. Zhu, Enhanced visible photocatalytic oxidation activity of perylene diimide/g-C3N4 n-n heterojunction via π-π interaction and interfacial charge separation, Applied Catalysis B: Environmental,

271 (2020) 118933.
[46] L. Lai, J. Yan, J. Li, B. Lai, Co/Al2O3-EPM as peroxymonosulfate activator for sulfamethoxazole removal: Performance, biotoxicity, degradation pathways and mechanism, Chemical Engineering Journal, 343 (2018) 676-688.
[47] J. Miao, Y. Yang, P. Cui, C. Ru, K. Zhang, Improving Charge Transfer Beyond Conventional Heterojunction Photoelectrodes: Fundamentals, Strategies and Applications, Advanced Functional Materials, 34 (2024).
[48] Z. Xing, J. Chen, S. Qin, X. Yang, Y. Ma, Y. Li, Oxygen-vacancy-engineered CoFe2O4 catalysts for degradation of tetracycline via peroxymonosulfate activation, Inorganic Chemistry Communications, 182 (2025).
[49] Y. Feng, D. Wu, Y. Deng, T. Zhang, K. Shih, Sulfate Radical-Mediated Degradation of Sulfadiazine by CuFeO2 Rhombohedral Crystal-Catalyzed Peroxymonosulfate: Synergistic Effects and Mechanisms, Environmental Science & Technology, 50 (2016) 3119-3127.
[50] S. Wang, L. Xu, J. Wang, Nitrogen-doped graphene as peroxymonosulfate activator and electron transfer mediator for the enhanced degradation of sulfamethoxazole, Chemical Engineering Journal, 375 (2019) 122041.
[51] C. Guan, J. Jiang, S. Pang, X. Chen, R.D. Webster, T.-T. Lim, Facile synthesis of pure g-C3N4 materials for peroxymonosulfate activation to degrade bisphenol A: Effects of precursors and annealing ambience on catalytic oxidation, Chemical Engineering Journal, 387 (2020) 123726.
[52] R. Guo, Y. Wang, J. Li, X. Cheng, D.D. Dionysiou, Sulfamethoxazole degradation by visible light assisted peroxymonosulfate process based on nanohybrid manganese dioxide incorporating ferric oxide, Applied Catalysis B: Environmental, 278 (2020) 119297.
[53] C. Guan, J. Jiang, C. Luo, S. Pang, Y. Yang, Z. Wang, J. Ma, J. Yu, X. Zhao, Oxidation of bromophenols by carbon nanotube activated peroxymonosulfate (PMS) and formation of brominated products: Comparison to peroxydisulfate (PDS), Chemical Engineering Journal, 337 (2018) 40-50.
[54] H.L. Lee, Z. Sofer, V. Mazánek, J. Luxa, C.K. Chua, M. Pumera, Graphitic carbon nitride: Effects of various precursors on the structural, morphological and electrochemical sensing properties, Applied Materials Today, 8 (2017) 150-162.
[55] C. Yang, S. Zhang, Y. Huang, K. Lv, S. Fang, X. Wu, Q. Li, J. Fan, Sharply increasing the visible photoreactivity of g-C3N4 by breaking the intralayered hydrogen bonds, Applied Surface Science, 505 (2020) 144654.

Supplementary Files

This is a list of supplementary files associated with this preprint. Click to download.

- Supplement.docx